



## Evaluation of gamma-ray transmission through rectangular collimator slits for application in nuclear fuel spectrometry

Lorenzo Senis<sup>a,\*</sup>, Vikram Rathore<sup>a</sup>, Anastasios Anastasiadis<sup>a,c</sup>, Erik Andersson Sundén<sup>a</sup>, Zsolt Elter<sup>a</sup>, Scott Holcombe<sup>b</sup>, Ane Håkansson<sup>a</sup>, Peter Jansson<sup>a</sup>, Daniel LaBrier<sup>c</sup>, Jason Schulthess<sup>d</sup>, Peter Andersson<sup>a</sup>

<sup>a</sup> Division of Applied Nuclear Physics, Department of Physics and Astronomy, Uppsala University, Sweden

<sup>b</sup> Institute for Energy Technology, Os Allé 5, NO 1777, Halden, Norway

<sup>c</sup> Idaho State University, Idaho Falls, ID, United States of America

<sup>d</sup> Idaho National Laboratory, Idaho Falls, ID, United States of America

<sup>e</sup> Swedish Radiation Safety Authority, SE 171 16, Stockholm, Sweden

### ARTICLE INFO

#### Keywords:

Gamma-ray spectrometry

Collimator efficiency

Irradiated fuel spectrum prediction

### ABSTRACT

Gamma-ray spectrometry is widely applied in several science fields, and in particular in non-destructive gamma scanning and gamma emission tomography of irradiated nuclear fuel. Often, a collimator is used in the experimental setup, to selectively interrogate a region of interest in the fuel. For the optimization of instrument design, as well as for planning measurement campaigns, predictive models for the transmitted gamma-ray intensity through the collimator are needed. Commonly, Monte Carlo radiation transport tools are used for accurate prediction of gamma-ray transport, however, the long computation time requirements when used in low-efficiency experimental setups present challenges.

In this work, the full-energy peak intensity transmitted through a rectangular collimator slit was examined. A uniform planar surface source emitting isotropically was considered, and the rate of photons reaching an ideal counter plane on the opposite side of the collimator was evaluated by analytical integration. To find a closed-form primitive function, some idealizations were required, and thereby parametric models were obtained for the optical field of view, dependent on slit dimensions (length, height and width) and source-to-collimator distance. It was shown that the count rate in the detector is independent of the collimator-to-source distance. For contributions from outside the optical field of view, where a closed-form expression cannot be found, instead fast numerical integration methods were proposed.

The results were validated using the Monte Carlo code MCNP6.2. For the analytical method, deviations were larger, the shorter the collimator, with up to 25% of underestimation obtained for the shortest examined collimator of 10 cm length. However, the longer the collimator, the better the observed agreement. This accuracy is deemed to be sufficient for instrument design and measurement planning, where often the order of magnitude of the count rate is not a priori known. For the numerical method, the results showed an agreement within 3% for all evaluated collimator settings.

The methods are planned for use in iterative optimization routines in the design of Gamma Emission Tomography devices, as well as for the prediction of gamma spectra obtained in the planning of fuel inspections. An application of the proposed method was demonstrated in spectrum prediction for a short cooling-time fuel rod test from the Halden reactor.

### 1. Introduction

Gamma-ray spectroscopy is a widely used technique in many fields of science. It is used in fundamental physics research as well as in various applications, ranging from medicine to nuclear technology. In this paper, the application of gamma-ray spectroscopy in non-destructive nuclear fuel inspections using e.g. gamma scanning [1] and in Gamma

Emission Tomography is addressed. In particular, the latter is increasingly considered for use in nuclear fuel tests as well as in nuclear safeguards [2–7]. The measurement systems in such cases include a detector with high energy resolution and a collimator, where the collimator provides the possibility to investigate well-defined regions of the fuel.

\* Corresponding author.

E-mail address: [lorenzo.senis@physics.uu.se](mailto:lorenzo.senis@physics.uu.se) (L. Senis).

<https://doi.org/10.1016/j.nima.2021.165698>

Received 17 May 2021; Received in revised form 16 July 2021; Accepted 28 July 2021

Available online 5 August 2021

0168-9002/© 2021 The Author(s). Published by Elsevier B.V. This is an open access article under the CC BY license

(<http://creativecommons.org/licenses/by/4.0/>).

The performance of a spectroscopic system is strongly impacted by the collimator design and therefore its geometric layout and material composition should be carefully evaluated during the initial stages of designing a spectroscopy system. Monte Carlo (MC) simulations are often used to provide results with the potential for good accuracy [8–10]. However, the MC technique exhibit the disadvantage of requiring large computational efforts to obtain sufficient statistical precision, especially if the collimator slit is narrow and long, causing a low probability for gamma rays to reach the detector. As an example, in the case of a square-slit collimator with dimensions of 0.1 cm wide and 80 cm long, the probability of a gamma ray to reach the opposite opening is on the order of  $10^{-9}$  for an isotropically emitting point source that is placed directly in front of the collimator opening. For the parts of a fuel object that are not directly in front of the opening, or further away, the probability of penetration can be substantially smaller. Consequently, MC techniques require a large number of sampled photons and may become prohibitively time consuming, unless dedicated variance reduction schemes are applied, such as suggested by [10]. In [10], a mono-directional source is modelled with the Monte Carlo radiation transport code MCNP6.2, and correction factors are introduced to solid-angle effects of isotropic emission and effects of finite volume in view of a cylindrical aperture.

This work aims to create fast computation models for calculation of the geometrical efficiency of detectors with rectangular-slit collimators, in order to replace time-expensive Monte Carlo gamma-ray transport simulations. Two approaches have been explored for this purpose, analytical integration of the optical field of view, while utilizing mathematical idealizations where needed, and numerical integration for more accurate response, including the transmission through the collimator bulk. Such methods will be used in iterative processes for design optimization of gamma-ray spectroscopy systems, and it is also anticipated to be used for the planning of experimental campaigns for transient tested fuel rods, similar to the work reported in [11].

The paper presents in the order that follows, models used to calculate the collimator efficiency, MCNP6.2 simulations used for validation, and a demonstration application of the models in spectrum prediction for a nuclear fuel rod.

## 2. Theory

For a given gamma-ray energy, the count rate,  $I_{CR}$ , in the detector of a spectroscopic system can be considered as a function of the source activity  $A$ , the emission intensity per decay of the gamma line  $I_\gamma$ , the geometric efficiency  $\epsilon_g$ , and the detector intrinsic full-energy peak efficiency,  $\epsilon_d$ , as expressed in Eq. (1),

$$I_{CR} = AI_\gamma \epsilon_g \epsilon_d. \quad (1)$$

Using this expression, the activity of a sample may be determined experimentally based on the number of counts in the full-energy peak of the gamma-ray spectrum. Notably, several correction factors may be required for accurate results, e.g., self-attenuation in the object, count-rate related effects, or true coincidence summing, depending on the measurement settings.

The geometry of the detector system studied in this work is schematically shown in Fig. 1, showing the use of a collimator; in our case, we consider for this a bulk of absorber material with a rectangular slit. The source and detector are for simplicity considered as simple planes. The geometric efficiency  $\epsilon_g$ , meaning the probability per photon to reach the detector, is in this case determined by the collimator slit dimensions and the collimator-source distance.

Generally, and as shown in Fig. 1, the collimator slit covers only a small fraction of the source plane. For this reason, it is more practical to express the count rate intensity based on the planar activity concentration of the source, adapted from [12], such as in Eq. (2) below:

$$I_{CR} = \int_{x_S} \int_{y_S} A_{sur} I_\gamma \epsilon_g(E_\gamma, x_S, y_S) \epsilon_d dx_S dy_S. \quad (2)$$

where  $A_{sur}$  refers to the surface activity concentration of the source plane in front of the collimator. The geometrical contribution to efficiency,  $\epsilon_g$  depends on the position of the source relative to the collimator, and thus needs to be expressed as a function of the source point. The geometrical efficiency depends also on the slit geometry and on the gamma-ray energy  $E_\gamma$  and may be expressed explicitly as:

$$\epsilon_g(E_\gamma, x_S, y_S) = \int_{x_D} \int_{y_D} \frac{\cos(\theta(x_S, y_S, x_D, y_D))}{4\pi R^2(x_S, y_S, x_D, y_D)} e^{-\mu(E_\gamma)k} dx_D dy_D, \quad (3)$$

where  $R$  is the distance travelled by a ray from a point on the source plane to the detector,  $E_\gamma$  is the gamma-ray energy,  $\theta$  is the angle between the emitted gamma ray and the normal to the detector plane, and  $k$  is the distance travelled by gamma-rays inside the collimator material, which depends on source plane coordinates  $(x_S, y_S)$  and the intersection with the detector plane  $(x_D, y_D)$ , where indices  $S$  and  $D$  refer to source and detector. It can be noted that the expression contains material and energy dependency through the linear attenuation coefficient,  $\mu$ , of the collimator bulk. The parameters  $R$  and  $\theta$  can be obtained explicitly from basic geometrical considerations:

$$R = \sqrt{(x_S - x_D)^2 + (y_S - y_D)^2 + (C + L)^2} \quad (4)$$

$$\theta = \arctan\left(\frac{\sqrt{(x_D - x_S)^2 + (y_D - y_S)^2}}{C + L}\right) \quad (5)$$

Finally, substituting the geometric efficiency of Eqs. (3)–(5) into Eq. (2) yields a quadruple integral expression for the expected count rate in the detector as:

$$I_{CR} = A_{sur} I_\gamma \epsilon_d \int_{x_S} \int_{y_S} \int_{x_D} \int_{y_D} \frac{\cos\left(\arctan\left(\frac{\sqrt{(x_D - x_S)^2 + (y_D - y_S)^2}}{C + L}\right)\right)}{4\pi((x_S - x_D)^2 + (y_S - y_D)^2 + (C + L)^2)} \times e^{-\mu(E_\gamma)k} dx_S dy_S dx_D dy_D. \quad (6)$$

The integrand in Eq. (6), which may be denoted as the collimator efficiency  $\epsilon_{col}$ , requires some simplification to yield a more trivial closed-form primitive function; these idealizations are discussed in the following sections.

The simplest case that we will first consider is that of the limit case  $\mu \rightarrow \infty$ , in which case Eq. (6) is greatly simplified. This limiting case can be considered as the optical contribution, since it corresponds to the transmission of optical light through a slit in an opaque absorber material. The optical field can be computed based on the integral in Eq. (6); however, it is practical to perform the integration in subsets of the source plane, as shown in Fig. 2 below.

The following source regions and respective contributions of the gamma-ray intensity at the detector position have been considered:

- The central contribution (CC), from the region directly in front of the slit opening,
- the penumbra contribution (PC), from parts of the source plane where the detector is partially in view through the slit,
- and finally, the total contribution (TC) that includes the whole source plane can be considered. This integration region is needed for the proper treatment also of gamma rays transmitted through the bulk material of the collimator.

### 2.1. The optical contribution

Considering first the central region contribution, the integral limits of Eq. (6) were adjusted to match the width and height of the slit,

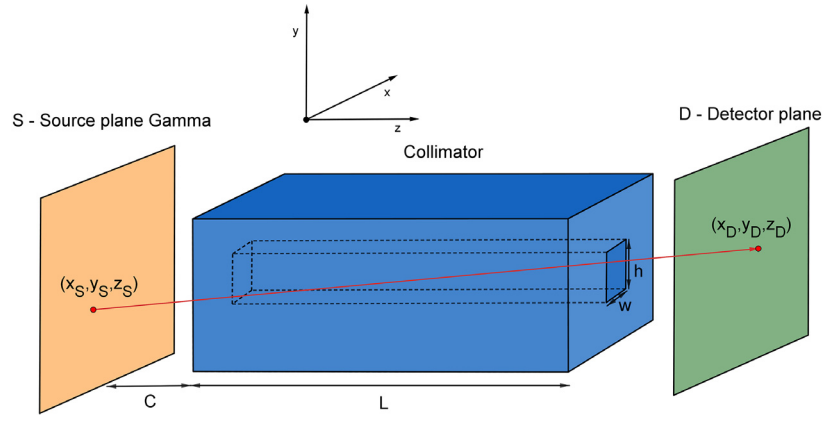


**Fig. 1.** Schematic representation of the setup in the considered configuration, which contains a source plane, a collimator with a rectangular slit, and a detector plane. An example of a gamma ray transmitted from a source point to a point in the detector is shown in red. (For interpretation of the references to colour in this figure legend, the reader is referred to the web version of this article.)

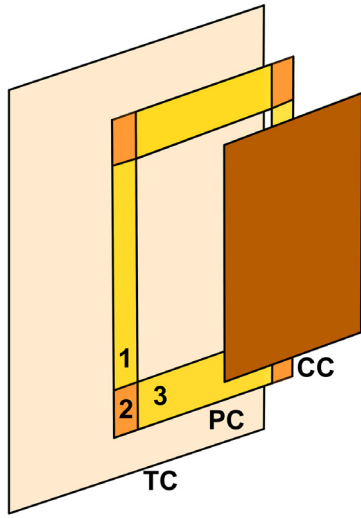


**Fig. 2.** Regions of integration on the source plane, used for the various contributions. CC: Central Contribution, PC: Penumbra Contribution (further divided in corners, 2 and sides, 1 and 3), and TC: Total Contribution (including gamma rays transmitted through collimator bulk material).

yielding the expression for the count rate contribution of the CC,  $I_{CC}$ , region as expressed in Eq. (7).

$$I_{CC} = A_{sur} I_{\gamma} \epsilon_d \int_{-\frac{w}{2}}^{\frac{w}{2}} \int_{-\frac{h}{2}}^{\frac{h}{2}} \int_{-\frac{w}{2}}^{\frac{w}{2}} \int_{-\frac{h}{2}}^{\frac{h}{2}} \frac{\cos\left(\arctan\left(\frac{\sqrt{(x_D - x_S)^2 + (y_D - y_S)^2}}{C+L}\right)\right)}{4\pi((x_S - x_D)^2 + (y_S - y_D)^2 + (C+L)^2)} dx_S dy_S dx_D dy_D, \quad (7)$$

where  $h$  and  $w$  are respectively the height and width of the slit.

To achieve a simpler and integrable mathematical expression, two further simplifications were made. Firstly, the slit length is in general much larger than the width or the height of the collimator slit,

$$(C+L)^2 \gg (x_D - x_S)^2 + (y_D - y_S)^2, \quad (8)$$

and consequently, the approximation below is valid,

$$\frac{1}{(x_D - x_S)^2 + (y_D - y_S)^2 + (C+L)^2} \approx \frac{1}{(C+L)^2}. \quad (9)$$

Secondly, because of the assumption in Eq. (8), the inclination angle on the detector plane,  $\theta(x_S, y_S, x_D, y_D)$ , is approximately zero, therefore

$$\cos(\theta(x_S, y_S, x_D, y_D)) = \cos\left(\arctan\left(\frac{\sqrt{(x_D - x_S)^2 + (y_D - y_S)^2}}{C+L}\right)\right) \approx 1 \quad (10)$$

Inserting expression (9) and (10) into (7) yields an expression for the gamma intensity at the detector plane that is simple enough to be integrated into an analytical expression for the central contribution,

$$I_{CC} \approx A_{sur} I_{\gamma} \epsilon_d \int_{-\frac{w}{2}}^{\frac{w}{2}} \int_{-\frac{h}{2}}^{\frac{h}{2}} \int_{-\frac{w}{2}}^{\frac{w}{2}} \int_{-\frac{h}{2}}^{\frac{h}{2}} \frac{dx_S dy_S dx_D dy_D}{4\pi(C+L)^2} = \frac{w^2 h^2 A_{sur} I_{\gamma} \epsilon_d}{4\pi(C+L)^2} \quad (11)$$

## 2.2. The penumbra contribution

For the penumbra contribution, the source plane was divided into eight regions (outside each of the four corners and four sides of the central region). The respective integration limits are illustrated in Fig. 3.

For the limits of the source integral,  $LimPC_S$ , the similarity of triangles, ABD and DEF of Fig. 3 can be used to derive the expression in Eq. (12), in the same way for the x and y direction (as exemplified for the y axis),

$$LimPC_{Sy} = \frac{h}{2} + \frac{hC}{L} = \frac{h(L+2C)}{2L}. \quad (12)$$

Similarly, for the integration limits in the detector plane,  $LimPC_D$ , were determined (see the example for the y-axis integration limits in Fig. 3). The limits were obtained using similarity relation between triangles, in this case triangles HGM and MNO of Fig. 3,

$$LimPC_{Dy} = \frac{h}{2} - (y_S - \frac{h}{2}) \frac{L}{C} = \frac{hC - 2y_S L + hL}{2C}. \quad (13)$$

Substitution of the limits into Eq. (6) yields three new integrals (and the respective primitives), for the penumbra regions PC<sub>1</sub>, PC<sub>2</sub> and PC<sub>3</sub>, where the index corresponds to the numbering used in Fig. 2:

$$I_{PC_1} \approx A_{sur} I_{\gamma} \epsilon_d \int_{\frac{w}{2}}^{\frac{w(1+2C)}{2L}} \int_{-\frac{h}{2}}^{\frac{h}{2}} \int_{-\frac{w}{2}}^{\frac{wC-2x_S L+wL}{2C}} \int_{-\frac{h}{2}}^{\frac{h}{2}} \frac{dx_S dy_S dx_D dy_D}{4\pi(C+L)^2} = \frac{w^2 h^2 C A_{sur} I_{\gamma} \epsilon_d}{8\pi L (C+L)^2}, \quad (14)$$

$$I_{PC_2} \approx A_{sur} I_{\gamma} \epsilon_d \int_{\frac{w}{2}}^{\frac{w(1+2C)}{2L}} \int_{\frac{h(1+2C)}{2L}}^{\frac{h}{2}} \int_{-\frac{w}{2}}^{\frac{wC-2x_S L+wL}{2C}} \int_{-\frac{h}{2}}^{\frac{hC-2y_S L+hL}{2C}} \frac{dx_S dy_S dx_D dy_D}{4\pi(C+L)^2}$$

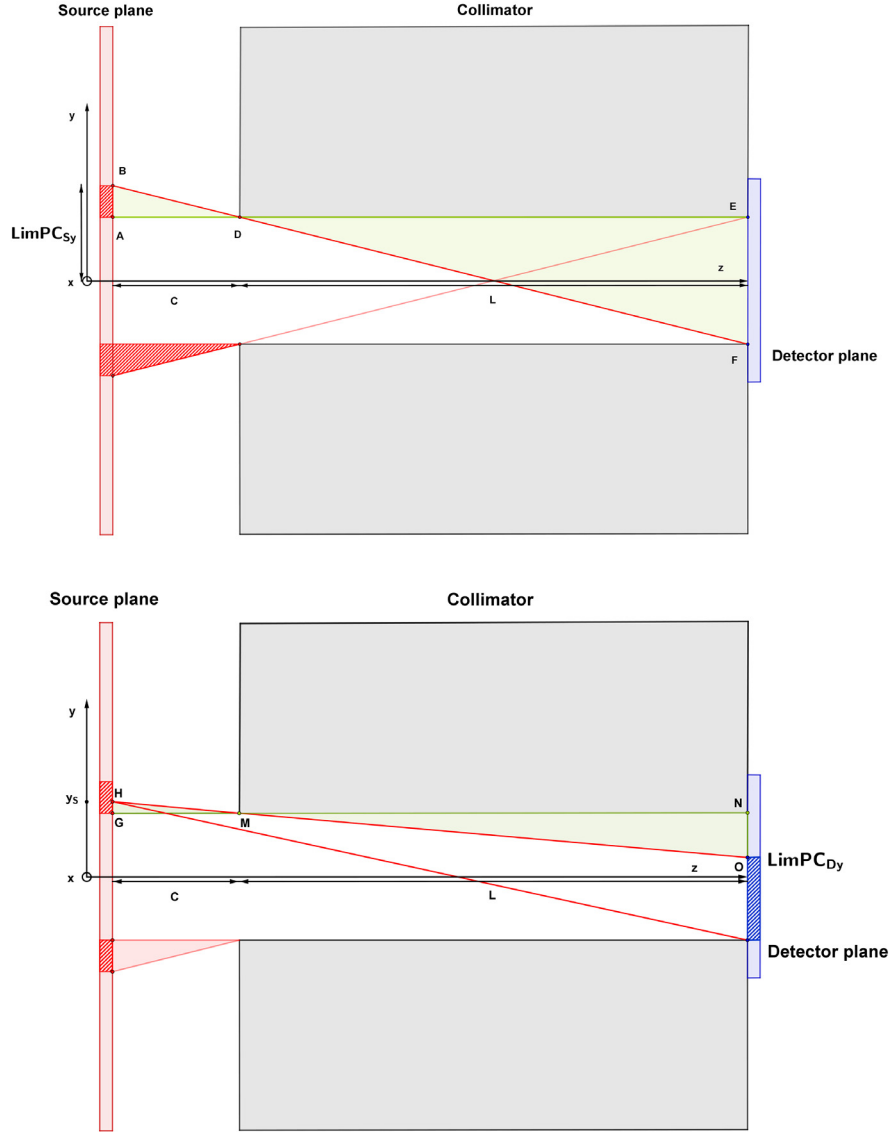


**Fig. 3.** Representation of the integration limits in the source and detector planes for the penumbra contribution to the optical field of view. It can be noted that in our analysis, the detector plane is assumed adjacent to the collimator back. However, the results would be equivalent for a larger separation, as long as the detector is large enough to cover the collimated beam.

$$= \frac{w^2 h^2 C^2 A_{sur} I_\gamma \epsilon_d}{16\pi L^2 (C + L)^2}, \quad (15)$$

$$I_{PC_3} \approx A_{sur} I_\gamma \epsilon_d \int_{-\frac{w}{2}}^{\frac{w}{2}} \int_{\frac{h}{2}}^{\frac{h(1+2C)}{2L}} \int_{-\frac{w}{2}}^{\frac{w}{2}} \int_{-\frac{h}{2}}^{\frac{hC-2y_S L+hL}{2C}} \frac{dx_S dy_S dx_D dy_D}{4\pi(C+L)^2} = \frac{w^2 h^2 C A_{sur} I_\gamma \epsilon_d}{8\pi L (C + L)^2}. \quad (16)$$

By summing equations (14), (15) and (16), a compact expression including all the eight PC regions is obtained:

$$I_{PC} = 2I_{PC_1} + 4I_{PC_2} + 2I_{PC_3} \approx \frac{A_{sur} I_\gamma \epsilon_d w^2 h^2 C (2L + C)}{4\pi L^2 (C + L)^2}. \quad (17)$$

### 2.3. The optical contribution

The optical contribution constitutes the sum of the central contribution and the penumbra contribution. Thus, by summing equations (11) and (17), the following compact expression for the Optical Contribution (OC) is obtained:

$$I_{CC} + I_{PC} \approx \frac{A_{sur} I_\gamma \epsilon_d w^2 h^2}{4\pi L^2}. \quad (18)$$

As evident in Eq. (18), the Optical Contribution is independent of the collimator-source distance,  $C$ .

### 2.4. The total contribution

For completeness, the calculation of the Total Contribution – which includes the transmission of gamma rays through the collimator bulk, and not only the optical field of view – was performed. However, it is noted that a convenient closed-form expression could not be found for finite  $\mu$ , since in this case the attenuation factor,  $e^{-\mu k(x_S, y_S, x_D, y_D)}$ , does not cancel out in Eq. (6).

For determination of  $k(x_S, y_S, x_D, y_D)$ , it was noted that the rectangular slit is defined by six boundary planes,  $P$ , two of which are normal to each coordinate axis,  $P_{x,1}$ ,  $P_{x,2}$ ,  $P_{y,1}$ ,  $P_{y,2}$ ,  $P_{z,1}$ ,  $P_{z,2}$ . In addition, the trajectory of a gamma ray from source point  $(x_S, y_S, 0)$  to detector point  $(x_D, y_D, L+C)$  defines a straight line  $L(x_S, y_S, x_D, y_D)$ . The planes  $P$  and the line  $L$  are used to calculate the distance,  $s$ , travelled inside the slit according to the following sequence of operations:

(1) First it is evaluated if the line  $L$  is parallel to any pairs of boundary planes  $P_x$ ,  $P_y$ , or  $P_z$ . If parallel planes exist, it is determined if  $L$  is always between the corresponding planes,

- a. If so, the intersections with the other non-parallel planes is determining the length of the trajectory inside the slit,  $s$ , according to step 2–7 below.
- b. If always outside, or in the improbable event where the line is in the boundary plane itself, the trajectory is judged as being outside the slit, and  $s = 0$ .

(2) Secondly, after removing any potential parallel boundary planes from consideration, the points of intersection of remaining non-parallel planes,  $P$ , and  $L$  are found, resulting in the existence of up to six intersection points. The distance from the source point  $(x_s, y_s, z_s)$  to each intersection is determined, and can be denoted  $s_{x,1}, s_{x,2}, s_{y,1}, s_{y,2}, s_{z,1}, s_{z,2}$ . These represent the entrance and exit from the slit space, listed by coordinate axis.

(3) A potential point of slit entry happens when the first plane of each boundary plane pair corresponding to each axis  $(x, y, z)$  has been intersected by  $L$ . The distance,  $s_1$ , to this point is determined by:

$$s_1 = \operatorname{argmax} \left( \operatorname{argmin} (s_{x,1}, s_{x,2}), \operatorname{argmin} (s_{y,1}, s_{y,2}), \operatorname{argmin} (s_{z,1}, s_{z,2}) \right). \quad (19)$$

(4) And similarly, a potential point of slit exit happens when the second boundary plane of any axis  $(x, y, z)$  has been intersected by  $L$ . The distance,  $s_2$ , to this point is determined by

$$s_2 = \operatorname{argmin} \left( \operatorname{argmax} (s_{x,1}, s_{x,2}), \operatorname{argmax} (s_{y,1}, s_{y,2}), \operatorname{argmax} (s_{z,1}, s_{z,2}) \right). \quad (20)$$

(5) If  $s_2 > s_1$ , there is overlap between the subspaces of  $L$  where each of the  $x$ ,  $y$ , and  $z$  coordinates are inside the slit. The distance  $s$ , travelled inside the slit is determined according to

$$s = \begin{cases} 0, & \text{if } s_2 < s_1 \\ s_2 - s_1, & \text{if } s_2 > s_1 \end{cases} \quad (21)$$

(6) The total distance travelled through the collimator as a whole,  $r$ , (which includes both the slit and the bulk material) is determined using the distance between intersections of the front and back plane of the collimator,  $r = s_{z,1} - s_{z,2}$ .

(7) Finally, the attenuating distance,  $k$ , travelled through the collimator bulk material is determined by difference of the total distance in collimator and the distance travelled inside the slit, according to  $k = r - s$ .

The steps 1–7 above were implemented in a MATLAB function, expressing  $k(x_S, y_S, x_D, y_D)$ . Since the aforementioned operations are not constituting an analytically integrable expression, a solution to the Total Contribution,  $I_{TC}$ , requires numerical approaches, and for this task Monte Carlo integration technique was used. It can be noted that while, in practice, this means a retreat to the Monte Carlo techniques that we set out to avoid, the random sampling is made of not only the source coordinates, as in traditional use of codes such as MCNP6.2 or Serpent2, but also by using a random sampling of the target coordinates of the gamma rays in the detector plane. As an effect, the computation speed can be expected to be improved by avoiding the efficiency losses due to solid angle effects.

The TC integration is performed by using a large number,  $N$ , of samples of the parameters  $(x_s, y_s, x_d, y_d)$  to estimate the average of the integrand in Eq. (6). It can be noted that this was performed without the small-angle approximation introduced in latter equations, and with the exponent  $k(x_S, y_S, x_D, y_D)$  substituted according to steps 1–7 above.

**Table 1**

Ranges used for parameters varied in the validation simulations.	
Parameter	Range of trials
Slit width, $w$	0.05 to 0.3 cm
Slit height, $h$	0.15 to 0.9 cm
Slit length, $L$	10 to 160 cm
Collimator to source distance, $C$	3 cm

The uncertainty,  $\sigma_{TC}$ , of the estimate was evaluated by using the sample standard deviation,  $s_{TC}$ , according to  $\sigma_{TC} = s_{TC}/\sqrt{N}$ .

### 3. MCNP6.2 validation simulations

To benchmark the analytical model for the optical field of view (OC) and the numerical integration model for the total transmitted contribution to the radiation (TC), simulations were performed using the well-validated Monte Carlo radiation transport simulation code MCNP6.2 [13]. For verification of the OC model, the importance of the collimator material (outside the slit) was set to zero. This causes truncation of any photon history that enters, in order to study only gamma rays with a source–detector propagation path inside the slit, as assumed in the derivation of the optical contribution. For verification of the TC model, the collimator was modelled as a solid block of tungsten (with density of 19 g/cm<sup>3</sup>) with a rectangular slit. Simulations were performed for various parameter sets ( $w$ ,  $h$ ,  $L$  and  $C$ ) using a source of 662 keV gamma rays (such as from <sup>137</sup>Cs), generating test data for the gamma intensity reaching the detector. In the MCNP6.2 code, the probability of the gamma ray to cross the detector plane was investigated using the F1 photon tally functionality [13], which yields the probability per starting photon. Thus, the results correspond to the geometric efficiency of the collimated detector, and can be compared to the results obtained by the OC and TC models derived above in Section 2. In MCNP6.2, the full energy (within 1 keV) was used for the evaluation, whereas some gamma rays may reach the detector as a low energy background were discriminated.

The attenuation coefficient of the collimator bulk is a required input to the TC model, and this may be retrieved from standardized databases such as NIST XCOM, [14]. However, for the validation of the proposed methods, care was taken to use the same attenuation coefficient in the TC model, as reflected by the cross sections and atomic density in the MCNP6.2 model (whereas it can be noted that the closed-form expression for the OC does not require this input). Since the attenuation coefficient is commonly listed either with or without the contribution from coherent scattering, both these options were evaluated.

In order to validate the performance of the derived collimator models, the MCNP6.2 output needs to be precise. A total of 61 simulations were performed with parameters in the range given in Table 1, with each set to terminate when reaching a relative precision of 0.1%, requiring in some cases a long time to be performed.

To speed up the MCNP6.2 simulations and to practically enable the simulation validation, source biasing techniques were used. In particular, the source emission angle was truncated to be exclusively inside a cone oriented in the direction of the detector. The central angle of the cone was set to a factor five larger than the largest possible inclination angle in the optical field and the closest source position ( $C = 0$  cm). In addition, the source and detector planes were extended outside the field of view of the collimator slit for a limited range. In each case, the truncation limits were set at a factor of five larger than the central region in front of the collimator slit. This truncation may introduce an inaccuracy, and therefore, separate simulations were performed outside each truncation limit, by investigating the result of an adjacent source outside the selected truncation limit, the results indicating that the bias error introduced due to truncation was about 1 permille or less, depending on the slit dimensions investigated, which was considered to be negligible.

**Table 2**

The collimator efficiency obtained by OC and TC models, compared with the MCNP6.2 results, for the shorter collimator test set (10 and 21 cm). The uncertainties expressed in parentheses are 1-sigma precisions of the Monte Carlo estimates.

Length of collimator [cm]	10			21		
	0.05	0.10	0.30	0.05	0.10	0.30
MCNP6.2 [ $s^{-1}$ ]	5.9541(60)E-08	9.5770(96)E-07	7.7128(85)E-05	1.1484(11)E-08	1.8488(18)E-07	1.5048(16)E-05
TC/MCNP6.2	0.9737(17)	0.9675(16)	0.9699(15)	0.9874(20)	0.9789(21)	0.9775(17)
TC (w.o. coherent)/MCNP6.2	0.9888(17)	0.9829(16)	0.9847(15)	0.9933(20)	0.9886(21)	0.9821(17)
OC/MCNP6.2	0.7520(10)	0.74802(81)	0.75202(83)	0.8842(13)	0.8787(14)	0.87439(92)

**Table 3**

The MCNP6.2 validation results of simulations of varied collimator length. It can be noted that the longer the slit, the more accurate the optical approximation. It can also be noted that overall the TC model is more accurate if the attenuation coefficient input is based on the photon cross sections without coherent scattering. The  $1\sigma$  Monte Carlo precision error estimates of the two last decimals are shown in parentheses.

Length of collimator [cm]	10	20	40	80	160
MCNP6.2 result (per starting photon)	4.241(13)E-7	9.076(27)E-8	2.1185(61)E-8	5.130(15)E-9	1.2643(37)E-9
Ratio TC/MCNP6.2	0.9781(77)	0.9945(94)	0.994(10)	0.998(11)	0.989(11)
Ratio TC (w.o. coherent)/MCNP6.2	0.9956(75)	1.0014(93)	0.997(10)	1.000(11)	0.990(11)
Ratio OC/MCNP6.2	0.7506(30)	0.8768(30)	0.9391(29)	0.9695(30)	0.9835(29)

## 4. Results

### 4.1. Verification of optical contribution

The simulation of the Optical Contribution shows that with varying slit width, the gamma current reaching the detector ranges over many orders of magnitude. A good overall agreement was noted with the MCNP6.2 simulations, including a perfectly absorbing collimator, and the derived model in Section 2.3, as shown in Fig. 4, with an average disagreement smaller than 0.3%. This indicates that the Optical Contribution is correctly calculated. It can be noted that the disagreement slightly increases with the increase of the slit width, due to the increasing importance of the small-angle approximation (see Section 2.1) for the accuracy. Note that the simulations have been run with the same starting seed, to better observe the trend of the intensity variations due to the geometry of the setup.

As shown in Fig. 4, the intensity decreases quite rapidly while moving to the smaller slit dimensions. This behaviour is well explained in Eq. (18) for the power of four dependence on the slit width (note that this holds for cases where  $w$  and  $h$  are related by a constant scaling factor).

### 4.2. Accuracy of derived models

The results of the MCNP6.2 validation simulations including the penetrating gamma component crossing the collimator bulk material, show that the derived models, OC and TC, are systematically underestimating the gamma intensity reaching the detector. This might have been expected, since MCNP6.2 may include contributions from small-angle scattered gamma rays. In particular the OC model has the largest deviation, which also might have been expected since the OC model neglects in addition any gamma-rays that penetrate the bulk material. It was found that the error of the OC model is decreasing with the length of the collimator. In the case of the tungsten collimator model studied, the underestimate is about 25% in the shortest collimator studied, of 10 cm length, and decreasing with collimator length. However, both models can predict the right order of magnitude of the collimator efficiency.

For the TC model, at the cost of longer computation time, as compared to the OC analytical integrals, the accuracy was seen to be substantially improved, as shown in Fig. 5. Deviations between the TC model and the MCNP6.2 reference was 2% or below (as reported in Table 2). It was found that this discrepancy was slightly larger when the attenuation coefficient included coherent scattering, resulting in a deviation of up to 3%. This might have been expected considering that coherent scattering does not affect the energy of scattered gamma photons, and only to a small extent their direction. Therefore, the

**Table 4**

The *FOM* results for the TC and MCNP6.2 simulations cases of Table 3.

Length of collimator [cm]	10	20	40	80	160
<i>FOM</i> MCNP6.2	1.66E+03	1.37E+03	1.30E+03	1.28E+03	1.24E+03
<i>FOM</i> TC	7.37E+03	4.44E+03	3.64E+03	3.49E+03	3.06E+03

scattered gamma ray may still be registered in the detector as a full energy event, so removing the coherent scattering from excluding the factor  $\mu$  factor leads to better accuracy.

For a 0.1 cm x 0.1 cm collimator (width x height), multiple tests were performed by varying the collimator length to reveal the dependence of the accuracy on the collimator length (up to 160 cm). The results show that while the optical model consistently underestimates the intensity, the discrepancy was smaller the longer the collimator. At 10 cm collimator length, the OC intensity was 75% as compared to MCNP6.2, while at 160 cm length, the ratio of the two was 98%. The results of the tests with the varied collimator length are shown in Fig. 6 and Table 3.

### 4.3. Notes on the computation time

To evaluate the time performance, we calculated a figure of merit, *FOM*, and compared the results between the different models. The figure of merit can be defined as a function of the computational time,  $T$ , and is the relative random error of the result,  $R$ , as  $FOM = \frac{1}{R^2 T}$  [15], and the higher is its value, the better is the code performance. The computation time needed per evaluation of the OC model was in the order of microseconds while not subject to random uncertainty. Because of this, the OC model has an infinite *FOM* value, and the negligible time for calculation makes the model suitable for iterative optimization routines. The computational time of the TC model (which requires numerical integration and where we used Monte Carlo sampling of source and detector points) was substantially slower. On the standard laptop used (Intel®Core™ i7-8650U CPU @1.90 GHz, 16GB RAM), and for the studied cases showed in Table 3, the time required was about 2 min per evaluation (for precision of 1%). The MCNP6.2 simulations were in the order of 3 times longer than the TC calculations (for the same precision and without scattering calculations). The reason for this is understood to be the solid angle effects: the TC integral uses random sampling of source and detector points, thereby never missing the detector, while on the contrary, many starting photons tracked in MCNP6.2 miss the detector (despite the source bias applied to truncate the emission cone in MCNP6.2, and the application of an energy cut just above the energy of emission, as described in Section 2). The results are shown in Table 4.

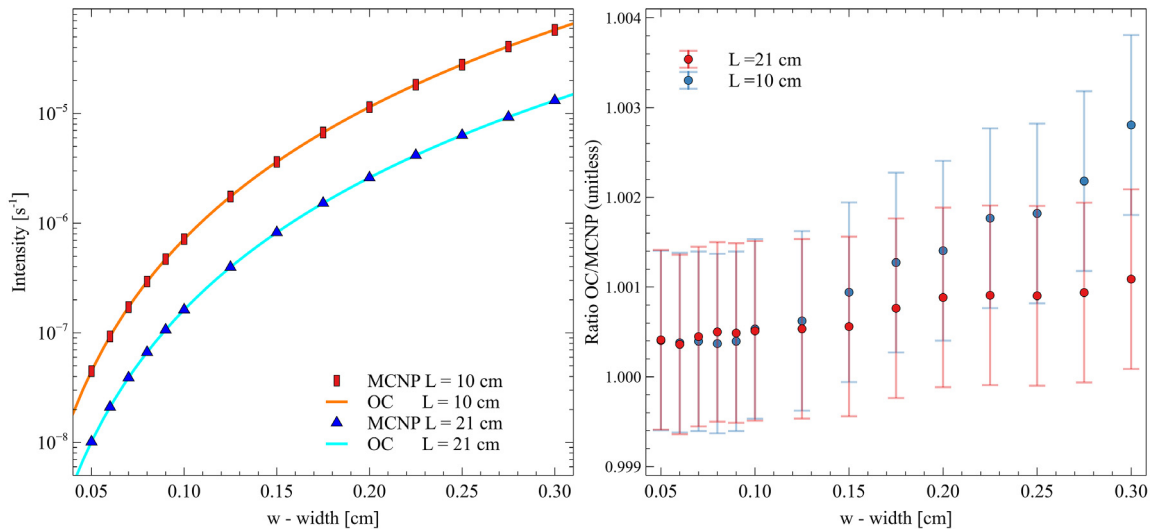


Fig. 4. Left: Comparison OC model with MCNP6.2 simulation of perfectly absorbing collimator material. Results for fixed  $C = 3$  cm and varied  $w$ , (note that  $h$  is also varied, corresponding to  $h = 3 * w$ ). The markers represent the MCNP6.2 results and the continuous curves the OC model of Eq. (18). The error bars are not reported as they are too small to be seen in the scale used. Right: Ratio of OC Model to MCNP6.2. A systematic overshoot (of a few permille) of the OC model is clear, and dependent on the slit dimension. Errorbars represent  $1\sigma$  uncertainty reported in MCNP6.2. It can be noted that the errors of neighbouring data points are correlated, due to the use of identical seed in the MCNP6.2 simulations.

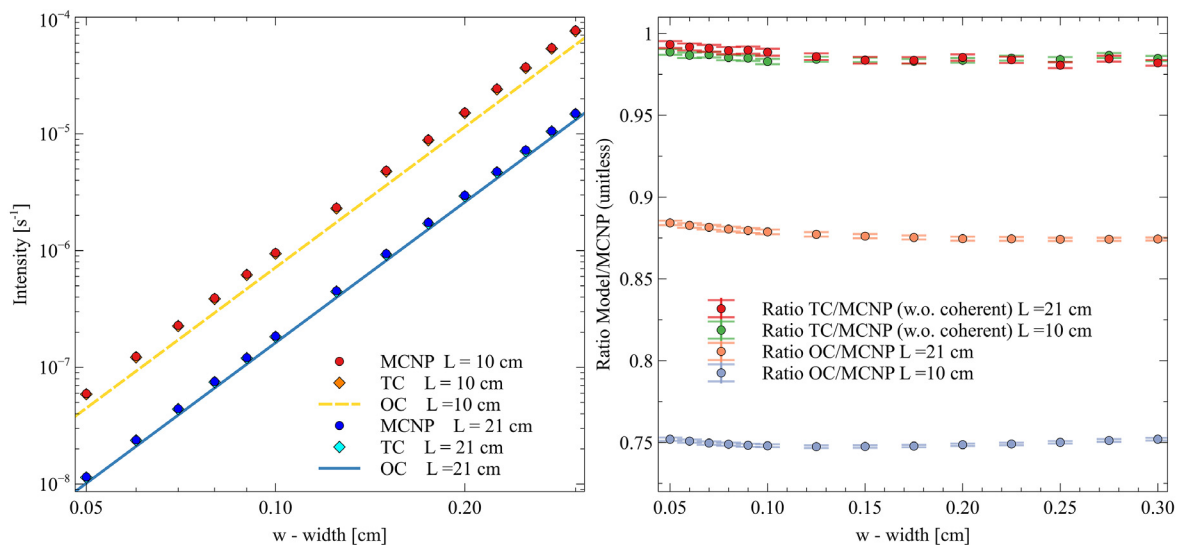


Fig. 5. Left: Comparison of absolute gamma-ray intensity at the detector plane between MCNP6.2 (including the penetrating gamma component) and models (TC and OC), with varied slit width and length. The error bars are not reported because of being too small to be seen. Right: Ratio of Models to MCNP6.2. A systematic undershoot of the OC model is clear, and strongly dependent on the collimator length. Errorbars are based on propagation of  $1\sigma$  estimates from MCNP6.2 and TC method.

It can be noted that the TC model shows a factor of 3 of improvement over the MCNP6.2 simulations, making the method more convenient. Both of the methods showed better performances for smaller slits. It can also be noted that even longer time was spent on simulations performed to investigate potential inaccuracy caused by the truncation limits of the source bias in MCNP6.2, as described in Section 3, which due to the low probability of reaching the detector took the longest time to reach the desired precision. However, these simulations were not included in the FOM of Table 4.

It should be remembered when comparing the computation time performance between OC, TC and MCNP6.2, that different level of accuracy is obtained, as seen in Section 3. The MCNP6.2 can realistically include transmission and scatter of gamma rays in the collimator bulk material, while the TC model only includes transmission of un-scattered gamma. In turn, the OC model includes no transmission except through the slit.

#### 4.4. Notes on the relative importance of Penumbra and Central regions

From the equations presented in Section 2.1, is possible to evaluate the relative importance of the PC and CC, by comparing their respective magnitudes. It can be noted that the further the source plane is from the collimator, the greater the importance of the PC compared to the CC. It can be shown using Eqs. (11) and (17) that the Central and Penumbra contributions are of equal magnitude at  $C = L(\sqrt{2} - 1) \approx 0.41L$ , as is shown in Fig. 7. Since one purpose of the collimator is to make the detector sensitive to a well-defined subset of the source in front of the aperture, it can be noted that the smaller the distance from the collimator to the source, the better.

#### 5. Demonstration of application in spectrum prediction

As a demonstration of a planned use, the collimator response has been applied to the prediction of a fuel spectrum from a Halden Boiling

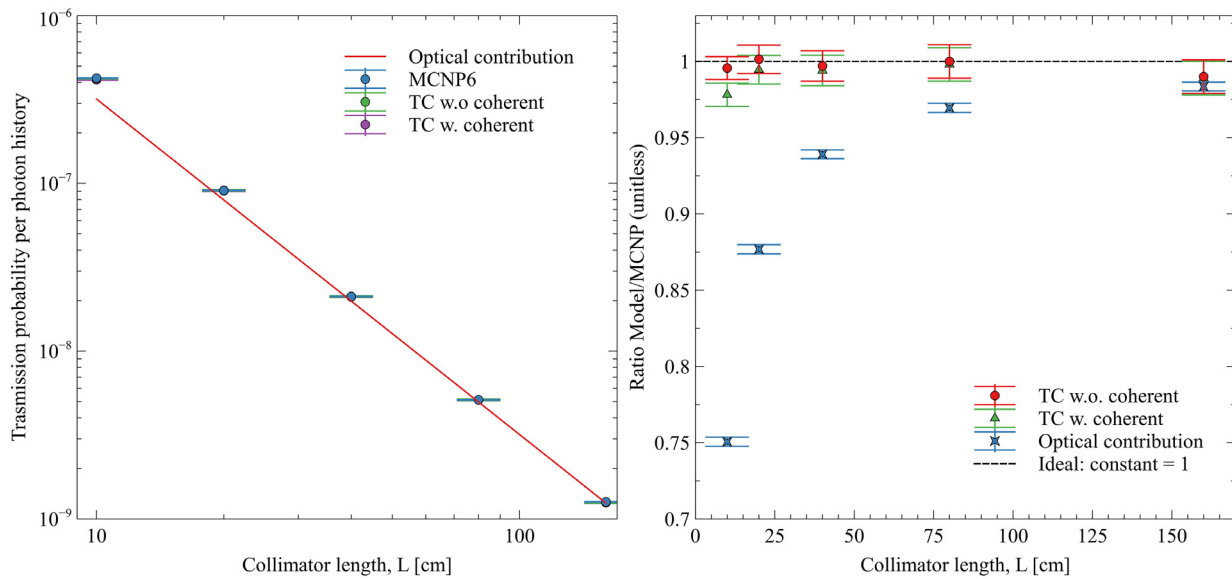


Fig. 6. Results of validation tests using long-slit collimators. Left: Absolute intensity of gamma-ray intensity. Right: The ratios of OC and TC models over the MCNP6.2 reference. Error bars correspond to 1-sigma precision error estimates from Monte Carlo estimates.

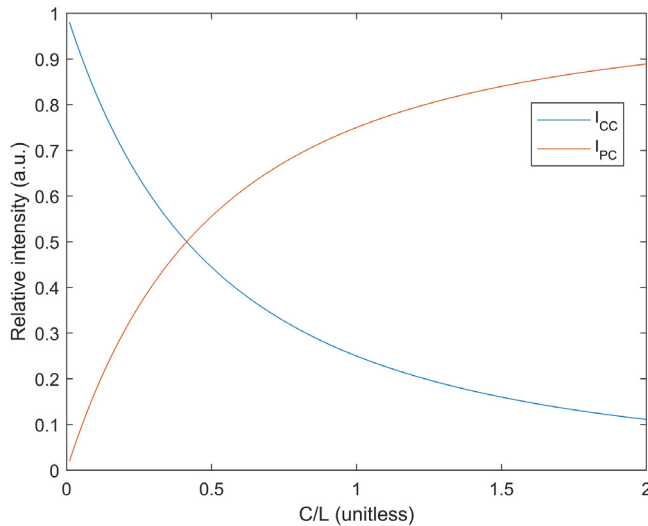


Fig. 7. The relative importance of the central and penumbra contributions varies with the distance from the source to the collimator. For small distances (compared to the collimator length), the central contribution dominates, while for distant sources, the dominating contribution is from the penumbra region.

Water Reactor (HBWR) LOCA transient test rod. Information about the measurement setup can be found in Ref. [16]. The irradiated fuel chosen for this was a single test rod irradiated with a highly unique burnup history, which comprises Pressurized Water Reactor irradiation and subsequently HBWR irradiation. In the first irradiation the fuel accumulated 60 MWd/kgU of burnup, distributed on 5 fuel cycles (from July 2000 to May 2005) and later stored for 12 years. Then, a smaller section of the original rod was obtained and the spectrum is acquired after a short cooling time of 14 days. Fuel rods such as this example are occasionally encountered in test reactors, where due to the special burnup history, or due to interest in an unusual nuclide, it may be difficult to beforehand know if the measurement is feasible, and which collimator size is appropriate to get sufficient (but at the same time not too high) count rate. We apply here the OC method to assess the spectrum and peak count rates, and compare them with the experimentally collected spectrum.

A fuel spectrum contains various radioactive nuclides and the activity of each needed to be considered. A multi-element vector  $A$  was defined, such that

$$A_{i=1:N} = [A_1, A_2, \dots, A_N] \quad (22)$$

where  $A_i$  is the activity of nuclide  $i$ , and  $N$  is the number of radioactive nuclide species contained in the irradiated fuel. The activity of all radioactive nuclides was provided by performing depletion calculations with Serpent2 [17], using a model of the fuel and its environment in the reactors. Two burnup simulations were modelled, one for each of the respective reactor used. The power history estimated at the fuel location was available and used in the Serpent2 burnup calculation.

The gamma rays emitted from the fuel can be categorized by the emission rate,  $S$ , and the gamma-ray energy,  $E$ . The energy is naturally discretized by the characteristic gamma lines of the nuclide inventory, such that  $E_j$  is a particular gamma emission energy, indexed by  $j = 1 : M$ , where  $M$  is the number of gamma lines from the irradiated fuel, and  $I_{\gamma_{i,j}}$  is the emission intensity of nuclide  $i$  at gamma energy  $E_j$ . This emission intensity was given by the Serpent2 output (although also available in nuclear data files). The emission intensity represents the number of emitted gamma rays at energy  $E_j$  per decay of nuclide  $i$ , where the total gamma source term,  $S_j$ , at energy  $E_j$  can be expressed as

$$S_j = \sum_{i=1}^N (A_i * I_{\gamma_{i,j}}) \quad (23)$$

This was multiplied by the geometric efficiency of the collimator,  $\epsilon_{col}$ , using the optical contribution model, in order to obtain the gamma-ray intensity at energy  $E_j$  that reaches the detector. For this, we utilized the collimator dimensions of 0.1 cm width and 0.2 cm height. For the length of the collimator, it can be noted that practical manufacturing considerations lead to the vertical and horizontal constraints of the slit were on different separation distance, at 65.5 cm and 75.5 cm respectively. For simplicity, we used the average of the two, at 70.5 cm, for the prediction of the spectrum.

The detector response has also a discretization because of the use of a multichannel analyser (MCA) with a discrete number of energy bins, indexed from  $k = 1 : K$ , where  $K$  is the number for channels used by the MCA. Due to the non-ideal response of a gamma-ray detector, the gamma rays are often detected at lower energy due to e.g. scattering with incomplete energy deposition. Because of this, the response

function of the detector is needed,  $Q_{k,j}$ , which is indexed by gamma ray energy  $j$  and MCA energy bin  $k$ . The elements of  $Q$  have been obtained by using Serpent2 simulation of a mono-directional source (mimicking the collimated beam) hitting a Canberra model GC2018, coaxial, P-type, HPGe detector [5]. The simulation was repeated one time for every source energy  $j$ , and for each simulation, the probability of deposition in MCA bin  $k$  was obtained. It can be noted that while the detector response required many simulations, one for each gamma ray energy, these are now relatively fast due to not including the inefficient collimators in the model, and therefore, every gamma ray hits the detector. By combining the detector response  $Q$  with the gamma intensity reaching the detector, the count rate,  $P_k$ , of MCA bin  $k$  was predicted according to Eq. (24). This calculation was repeated for  $k = 1 : K$ , for the calculation of the entire pulse height spectrum.

$$P_k = tD \sum_{j=1}^M (\epsilon_{col} S_j * Q_{k,j} * C_j) \\ = tD \epsilon_{col} \sum_{j=1}^M \left( \sum_{i=1}^N (A_i * I_{r,i}) * Q_{k,j} * C_j \right) \quad (24)$$

where  $t$  is the measurement time used, and  $C$  and  $D$  are correction factors.  $C_j$  is the correction for the self-attenuation in the fuel object and any structural material blocking the path of the gamma ray for gamma energy  $j$ . It was calculated based on the consecutive attenuation according to Beer–Lambert’s law, in the materials blocking the path of the gamma rays from the nuclear fuel to the detector, such as

$$C_j = e^{-\sum_m \mu_{m,j} x_m} \quad (25)$$

where  $m$  is an index for each material crossed by the path of the radiation in the fuel and instrument structures, which included a shroud, a heater cylinder wall, as well as the fuel itself. For the fuel, the distance travelled was approximated by the pellet radius.

It can be noted that the self-attenuation in the fuel pellet may be difficult to predict for transient test rods, due to the possibility of strong fuel relocation in transient test rods, fragmented fuel may evacuate from parts of the fuel stack, or conversely accumulate at regions of massive cladding strain. For the latter cases, the activity strongly increases in such locations as seen in Ref. [11], and the count rate can consequently be expected to vary as a consequence of the relocation. In this work, the spectrum was evaluated for pellets sited on the top of the rodlet, where the fuel fragmentation was expected to be small. For this reason, we assumed no relocation.

The other correction factor,  $D$ , expressed in Eq. (24), was needed for conversion of the activity concentration obtained by Serpent2, that is per unit length [Bq/cm], to a planar activity concentration in front of the collimator [Bq/cm<sup>2</sup>].

$$D = \frac{2}{\pi R_{pellet}} \quad (26)$$

The resulting spectrum was compared with a 30 s measurement, as shown in Fig. 8. It can be noted that the measured spectrum has been background subtracted using a background measurement performed with the collimator outside the fuelled region. A Gaussian broadening was also applied to each bin in the predicted spectrum. The Full Width Half Maximum of the Gaussian broadening was calculated using a linear fit over the energy interval of the spectrum using the expression presented in Table 6.4 in Ref. [18],  $a + bE$ , where  $a = 0.992$  and  $b = 7.14 \cdot 10^{-4}$ . A counting noise was also added, sampled from the Poisson distribution and added to each bin. This was done to provide comparable results between the predicted and the experimental data. Table 5 shows a comparison of predicted and measured peak intensities, showing that the method is able to predict the order of magnitude correctly for the peak intensities. However, as seen in Fig. 8, the continuum background is underestimated using this simplified approach.

## 6. Conclusions and discussion

Computation models were developed for collimator efficiency for gamma radiation, with the focus on achieving faster models than full Monte Carlo transport. Such models are planned to facilitate the planning of experiments, and for design and optimization of new gamma-spectrometric instruments, by allowing for iterative optimization routines. An analytical solution for the optical contribution (OC) is proposed to quantify the transmission through a rectangular collimator slit, where the limitation to the optical field of view constitutes an idealization of the full realistic transport, by neglecting transmission through material and build-up of scattered photons.

Validation using Monte Carlo transport code MCNP6.2 showed that the OC model is able to predict the correct order of magnitude of the collimator efficiency. A consistent underestimation of the peak intensity was shown, which can be up to tens of percent for shorter collimators of 10 cm. For longer collimators, the inaccuracy was observed to decrease to less than 2% in the case of 160 cm length. These levels of accuracy are judged to be sufficient for instrument design and experiment planning.

For potential applications where greater accuracy is needed, a model for prediction of the total contribution (TC), including also transmission through collimator bulk was proposed. This model obtained agreements with the MCNP6.2 validation data of less than 3%, consistently over the modelled parameter range. Although numerical integration with the Monte Carlo method is required in the TC model, it was found that it allowed for speed up by a factor of 3 as compared to the full Monte Carlo gamma transport simulation using MCNP6.2, even though variance reduction techniques and energy cut were applied. In addition, it was shown that slightly improved accuracy was obtained by using the linear attenuation coefficient without coherent scattering.

A potential application in spectrum prediction for test fuels spectra at research reactors was demonstrated, using data from a Halden test rod. It was shown that the peak intensities agree within tens of percent between prediction and experimental results. This is again accurate enough for use of the methods in the planning of experiments and design optimization. However, it is noted that further work is needed for the accurate prediction of the continuum background. The continuum background may be composed largely of scattered gamma-rays (i.e. build-up) from the fuel object itself as well as from the collimator and other parts of the setup. Since the continuum background may strongly affect the precision of a gamma-ray peak, further work is needed in order to improve its accuracy in the spectrum prediction models.

### CRedit authorship contribution statement

**Lorenzo Senis:** Conceptualization, Methodology, Software, Investigation, Data curation, Validation, Visualization, Formal analysis, Writing – original draft. **Vikram Rathore:** Resources, Conceptualization, Writing – reviewing & editing. **Anastasios Anastasiadis:** Writing – reviewing & editing. **Erik Andersson Sundén:** Supervision. **Zsolt Elter:** Resources, Writing – reviewing & editing. **Scott Holcombe:** Writing – reviewing & editing. **Ane Håkansson:** Supervision, Writing – reviewing & editing, Funding acquisition. **Peter Jansson:** Supervision, Resources, Writing – reviewing & editing. **Daniel LaBrier:** Writing – reviewing & editing. **Jason Schulthess:** Writing – reviewing & editing. **Peter Andersson:** Supervision, Conceptualization, Funding acquisition, Software, Resources, Data curation, Writing – original draft, Writing – reviewing & editing.

### Declaration of competing interest

The authors declare that they have no known competing financial interests or personal relationships that could have appeared to influence the work reported in this paper.

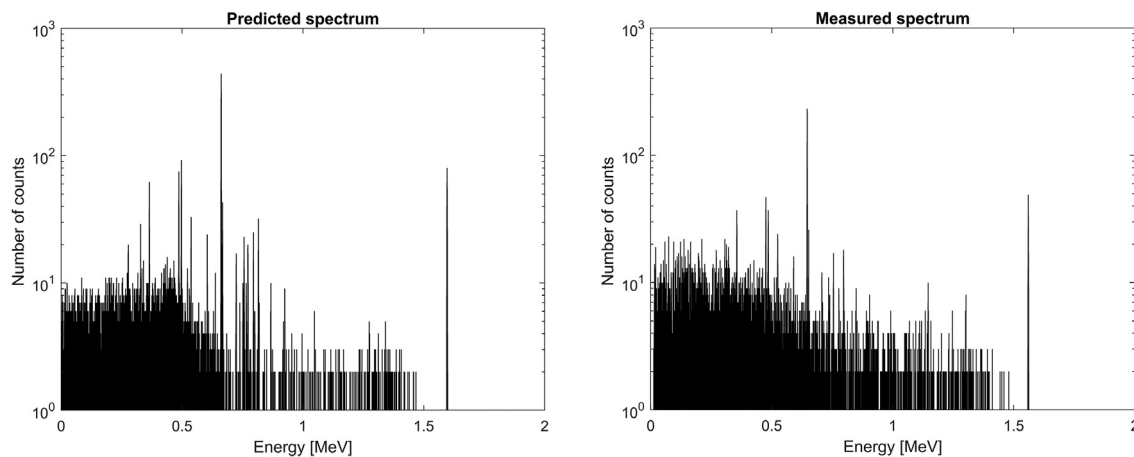


Fig. 8. Left: A 30 s pulse height spectrum as predicted using Eq. (24). Right: the measured spectrum of the modelled test fuel. While the peaks are reminiscent in magnitude, the continuum background is clearly underestimated in the predicted spectrum.

Table 5

Comparison of predicted peak intensities and measured data. Note that a background spectrum recorded in an unfueled region was subtracted from the experimental spectrum prior to the comparison. Uncertainties are based on counting errors in peak and background in the experimental data.

Nuclide/energy/half-life	Predicted number of counts	Experimental number of counts	Ratio Prediction/Experiment
<sup>137</sup> Cs/662 keV/30 a	740.6	739 ± 35	1.00 ± 0.05
<sup>140</sup> La /1596 keV/2 d	161.7	164 ± 13	0.99 ± 0.08
<sup>140</sup> La/486 keV/2 d	105.2	134 ± 21	0.79 ± 0.12
<sup>103</sup> Ru/497 keV/39 d	126.6	122 ± 22	1.04 ± 0.19
<sup>134</sup> Cs/604 keV / 2 a	37.93	38 ± 17	1.00 ± 0.45
<sup>140</sup> La/815 keV/2 d	54.56	43 ± 14	1.27 ± 0.41

## Acknowledgement

This work was financially supported by the Swedish Foundation for Strategic Research, grant number EM-16-0031.

## References

- [1] C. Willman, A. Håkansson, O. Osifo, A. Bäcklin, S. Jacobsson Svärd, Nondestructive assay of spent nuclear fuel with gamma-ray spectroscopy, *Ann. Nucl. Energy* 33 (2005) 427–438, <http://dx.doi.org/10.1016/j.anucene.2005.12.005>.
- [2] R. Virta, R. Backholm, T.A. Bubba, T. Helin, M. Moring, S. Siltanen, P. Dendooven, T. Honkamaa, Fuel rod classification from Passive Gamma Emission Tomography (PGET) of spent nuclear fuel assemblies, 2020, URL <https://arxiv.org/abs/2009.11617>.
- [3] P. Jansson, S. Jacobsson Svärd, A. Håkansson, A. Bäcklin, A device for nondestructive experimental determination of the power distribution in a nuclear fuel assembly, *Nucl. Sci. Eng.* 152 (1) (2006) 76–86, <http://dx.doi.org/10.13182/NSE06-A2565>.
- [4] C. Stefano, Characterisation of high-burnup LWR fuel rods through gamma tomography, *École Polytechnique Fédérale de Lausanne, Lausanne, Switzerland*, 2007, URL: <https://infoscience.epfl.ch/record/100031>.
- [5] S. Holcombe, S. Jacobsson Svärd, L. Hallstadius, A novel gamma emission tomography equipment for enhanced fuel characterization capabilities within the OECD Halden Reactor Project, *Ann. Nucl. Energy* 85 (2015) 837–845, <http://dx.doi.org/10.1016/j.anucene.2015.06.043>.
- [6] J. Schulthess, N. Woolstenhulme, A. Craft, J. Kane, N. Boulton, W. Chuirazzi, A. Winston, A. Smolinski, C. Jensen, D. Kamerman, D. Wachs, Non-destructive post-irradiation examination results of the first modern fueled experiments in TREAT, *J. Nucl. Mater.* 541 (2020) 152442, <http://dx.doi.org/10.1016/j.jnucmat.2020.152442>.
- [7] S. Shiba, H. Sagara, Passive gamma emission tomography with ordered subset expectation maximization method, *Ann. Nucl. Energy* 150 (2021) 107823, <http://dx.doi.org/10.1016/j.anucene.2020.107823>.
- [8] E.L. Smith, S. Jacobsson, V. Mozin, P. Jansson, A Viability Study of Gamma Emission Tomography for Spent Fuel Verification: JNT 1955 Phase I, Technical Report, PNNL-25995, 2016, URL <http://urn.kb.se/resolve?urn=urn:nbn:se:uu:diva-306584>.
- [9] T. Kähkönen, Evaluating the Viability of Serpent in Passive Gamma Emission Tomography (PGET) Radiation Transport Simulations, Special Assignment Report, Aalto University, Finland, 2021, URL <https://aaltodoc.aalto.fi:443/handle/123456789/102716>.
- [10] S. Kilby, Z. Jin, A. Avachat, et al., A source biasing and variance reduction technique for Monte Carlo radiation transport modeling of emission tomography problems, *J. Radioanal. Nucl. Chem.* 320 (2019) 37–45, <http://dx.doi.org/10.1007/s10967-019-06457-1>.
- [11] P. Andersson, S. Holcombe, T. Tverberg, Inspection of a LOCA test rod at the Halden Reactor Project using gamma emission tomography, in: *Top Fuel - LWR Fuels with Enhanced Safety and Performance*, American Nuclear Society, 2016, <http://urn.kb.se/resolve?urn=urn:nbn:se:uu:diva-303810>.
- [12] S. Jacobsson Svärd, Tomographic Measurement Technique for Irradiated Nuclear Fuel Assemblies, *Acta Universitatis Upsaliensis, Uppsala*, 2004, URL <http://urn.kb.se/resolve?urn=urn:nbn:se:uu:diva-4227>.
- [13] C.J. Werner, *MCNP Users Manual - Code Version 6.2, Report la-UR-17-29981*, Los Alamos National Laboratory, 2017.
- [14] M.J. Berger, J.H. Hubbell, S.M. Seltzer, J. Chang, J.S. Coursey, R. Sukumar, D.S. Zucker, K. Olsen, XCOM: Photon Cross Section Database (version 1.5), Gaithersburg, 2020.
- [15] J.K. Shultis, R.E. Faw, *An MCNP primer*, Manhattan, KS 66506, 2005-2011.
- [16] S. Holcombe, P. Andersson, Gamma emission tomography measurements of fuel assemblies at the Halden reactor, in: *Top Fuel - LWR Fuels with Enhanced Safety and Performance*, American Nuclear Society, Boise, Idaho, USA, 2016, URL <http://urn.kb.se/resolve?urn=urn:nbn:se:uu:diva-303812>.
- [17] J. Leppänen, et al., The serpent Monte Carlo code: Status, development and applications in 2013, *Ann. Nucl. Energy* 82 (2015) 142–150, *The Serpent Monte Carlo code: Status, development and applications in 2013*.
- [18] G.R. Gilmore, *Practical Gamma-Ray Spectroscopy*, Nuclear Training Services Ltd, Warrington, UK, Wiley, 2008.